Small Structures

small structures

www.small-structures.com

RESEARCH ARTICLE OPEN ACCESS

Explaining the Binding Puzzle of N-Heterocyclic Carbenes on Oxide Surfaces by Means of Density Functional Theory Calculations

Maria Voccia | Sergio Tosoni

Department of Materials Science, University of Milan-Bicocca, Milan, Italy

Correspondence: Sergio Tosoni (sergio.tosoni@unimib.it)

Received: 16 April 2026 | **Revised:** 14 September 2026 | **Accepted:** 6 October 2026

Keywords: adsorption | covalent functionalization | density functional theory | mesoionic carbene | N-heterocyclic carbenes | surface oxide

ABSTRACT

N-Heterocyclic carbenes (NHCs) have been successfully employed as ligands for the modification of metallic surfaces. Their adsorption on oxide surfaces remains less explored. Here we show, by means of density functional theory calculations, how five model NHCs bind covalently to different oxide surfaces, spanning from ionic (MgO) or covalent (SiO_2) large-gap oxides to small-gap TiO_2 and Cu_2O. A complex trend emerges, where NHCs are adsorbed only on positively charged surface sites on MgO and SiO_2, while both metal cations and oxygen anions can coordinate the molecules on Cu_2O and TiO_2. On Cu_2O, however, bonding on Cu sites is more favorable, while the opposite is found for TiO_2. The key aspect is that the bond to metal cations (or silicon) involves little charge transfer, while the bond to O implies a substantial electron donation to the oxide surface. The reducibility of the oxide and the alignment between its band edges and the NHC frontier orbitals are thus the determining factors for understanding this behavior.

1 | Introduction

N-Heterocyclic carbenes (NHCs) are gaining attention as promising organic building blocks for self-assembly and functionalization on metal surfaces [1–5], beyond their previous wide use in homogeneous catalysis [6, 7] and coordination chemistry [8–10]. NHCs are strong electron-donating ligands and can coordinate covalently to metals. The extension of their metal-bonding capability to extended metal surfaces or nanoparticles led to the recent application of NHCs in heterogeneous catalysis [10, 11]. An alternative approach for the application of NHCs-transition metal complexes in the context of heterogeneous catalysis consists of their immobilization on solid supports [12], such as oxide nanoparticles [13–15]. The NHC-functionalized materials so obtained have found promising applications in heterogeneous catalysis [10, 13–15], biosensing [16, 17], and microelectronics [18–20].

NHCs encompass a broad class of molecular structures [5, 10]. Among them, in Figure 1, one can distinguish between normal NHCs, where the presence of two nonbonding electrons on a C atom does not lead to formally charged species within the ring, and mesoionic carbenes [21] (MICs), where, on the contrary, neutral resonance forms are forbidden, and the carbene C atom bears a formal negative charge. The latter can be further divided into remote and nonremote NHCs, based on the position of the positive countercharge: in remote mesoionic NHCs, this is located in the meta- or para-position with respect to the carbene C. Among these molecules, the 1,2,3-triazol-5-ylidene class of MICs is particularly important since they can be readily prepared via "click" methods, and they possess strong σ-donor properties [22, 23]. Despite this, MICs have received little attention in the area of surface chemistry [24]. A further promising class of NHCs consists of polydentate carbenes, where two- or more N-heterocycles bearing carbene centers are connected via an alkyl chain, as shown in Figure 1. Analogous to other classes of ligands, polycarbenes display superior stability in complexing metal ions, thanks to the chelating effect [9, 25–27].

This is an open access article under the terms of the Creative Commons Attribution License, which permits use, distribution and reproduction in any medium, provided the original work is properly cited.

© 2026 The Author(s). *Small Structures* published by Wiley-VCH GmbH.

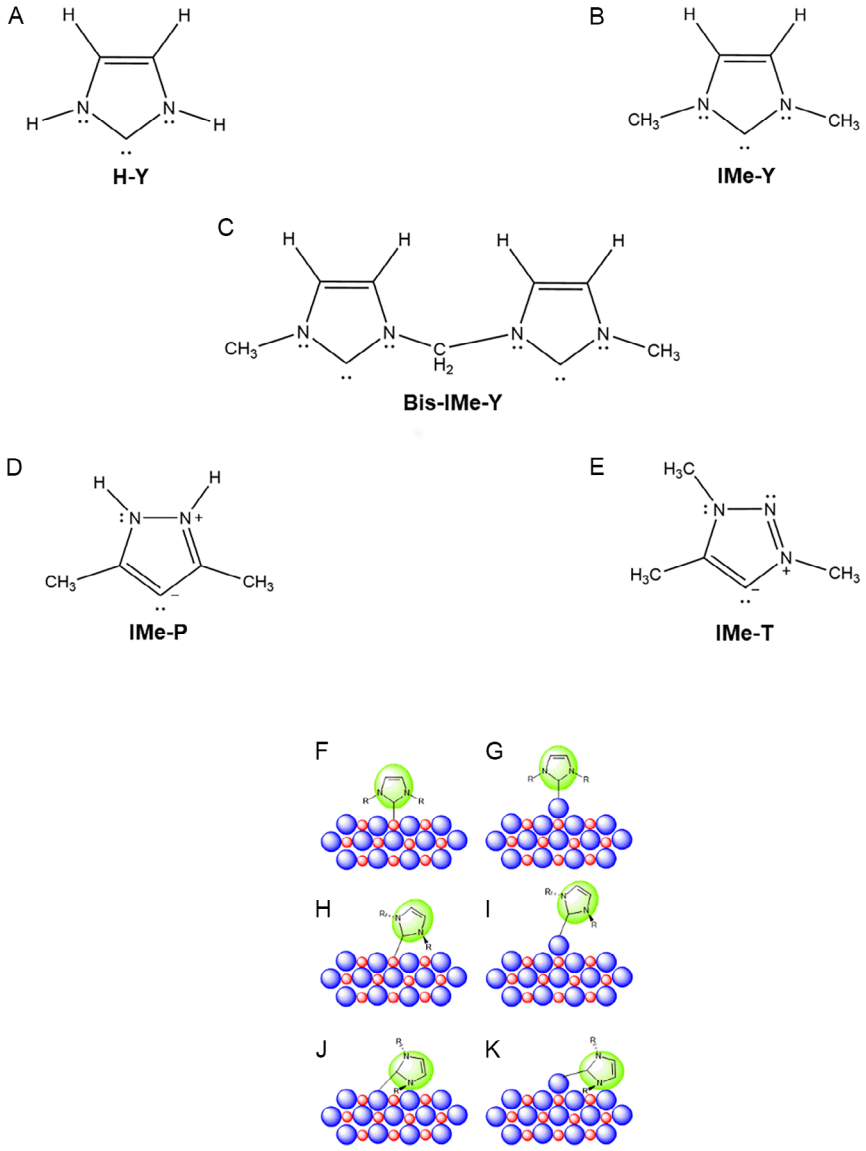


FIGURE 1 | Schematic representation of the molecular structures: (A) 4-imidazolin-2-ylidene (H-Y), (B) 1,3-dimethyl-4-imidazolin-2-ylidene (IMe-Y), (C) bis(3-methyl-4-imidazolin-2-ylidene-1-yl)methane (Bis–IMe-Y), (D) 3,5-dimethylpyrazolium-4-ide (IMe-P) and (E) 1,3,4-trimethyl-1,2,3-triazolium-5-ide (IMe-T). Schematic representation of the possible adsorption sites (Mg, Si, Cu, or Ti atoms in blue, oxygen atoms in red): (F) upright surface, (G) upright adatom, (H) tilted surface, (I) tilted adatom, (J) down-surface, (K) down-adatom.

Beyond their capability to strongly bind metals, both in the form of isolated ions and extended surfaces, NHCs have also been deposited on oxidized metal surfaces, with promising results in promoting the thermal reduction of the surface [28, 29]. The deposition of NHCs on oxidized metal surfaces or metal oxide thin films grown on metals revealed a somewhat surprising result: in some cases, NHCs were preferentially bound to oxygen anions rather than metal cations, despite the strong coordinating capability of these molecules toward metals. This was first observed experimentally and theoretically on oxidized Cu [30], while later an experimental report showed that a fluoride imidazolium NHC salt was bound to O on CuO_x thin films, to Ti on TiO_x films, and to both Fe and O atoms on FeO_x films [31, 32]. The different binding modes were related to changes in the electronic configurations of the metal cations in the metal oxide films, but no direct proof from electronic structure calculations was provided. NHC adsorption was also reported via O—H—C bonding on hydroxylated indium tin oxide surfaces [33]. Furthermore, the presence of NHCs was also proven on silica surfaces after spillover of NHC-M_1 complexes (M = Au and Cu) from NHC-decorated metal nanoparticles [34, 35] or generation *via* on-site reaction from organic precursors adsorbed on alumina [36].

This complex behavior requires a rationalization, which this work aims to provide by studying, with high-quality hybrid density functional theory (DFT) calculations, the adsorption of five NHCs (including normal, mesoionic, and bidentate NHCs, Figure 1) on simple model surfaces of four oxides: SiO_2, MgO, Cu_2O, and TiO_2. The selection of oxidic supports includes ionic (magnesia, cuprite, and, partially, titania) and covalent oxides (silica), as well as reducible (cuprite and titania) and nonreducible (magnesia and silica) oxides. Among the reducible supports, we chose a charge-transfer oxide (titania) and a Mott–Hubbard oxide (cuprite). It is thus interesting to see how the interplay of

26804062, 2026, 10, Downloaded from https://onlinelibrary.wiley.com/doi/10.1002/sstr.70647 by CochraneItalia, Wiley Online Library on [23/10/2026]. See the Terms and Conditions (https://onlinelibrary.wiley.com/terms-and-conditions) on Wiley Online Library for rules of use; OA articles are governed by the applicable Creative Commons License

these various factors determines the stability and the binding modes of NHCs. These selected oxides, moreover, have both fundamental and applicative relevance. MgO is, perhaps, a paradigm for model studies in heterogeneous catalysis [37]. Despite its structural simplicity and chemically inert character, the interplay between Lewis acidic (Mg^{2+}) and basic (O^{2-}) sites gives rise to strong interactions with organic and inorganic molecules. Copper is among the most studied metals in state-of-the-art electrocatalysis due to its low cost, abundance, and remarkably active nature, in reactions of paramount relevance such as CO_2 reduction [38]. Often, though, copper surfaces undergo partial oxidation, which makes copper oxide an interesting case study. Oxidized Cu surfaces, as mentioned above, have already been studied as a support for adsorbing NHCs. We hereby assume that results on cuprite (111) can be of direct interest in this respect, despite the much simpler structure of the model adopted here. Another interesting research field aiming at the optimization of Cu electrochemical and chemical performance concerns its coating with insulating thin films. As reported by some of us, silica thin films exhibiting a regular honeycomb-like hexagonal surface morphology can be extensively grown on oxidized Cu [39]. The free-standing silica bilayer studied here exhibits an analogous surface structure, thus providing information of high value for understanding the NHCs–silica film interactions. Titania, finally, is among the most studied materials for catalytic and photocatalytic applications. TiO_2 functionalization with organic molecules is also of great interest for theranostic applications. Studying the NHC–titania interactions at a fundamental level can be of high interest for the design of stable photoactive or biocompatible structures if one imagines that substituted NHCs could be prepared, bearing tailored functional groups.

Some inherent limitations of the models adopted here should be kept in mind. In this work, only ideal, flat, and defect-free oxide surfaces are considered. The role of point defects such as oxygen vacancies, very common in reducible oxides, or extended defects such as steps, will be the subject of forthcoming investigations. Different synthesis and deposition protocols, moreover, can lead to different binding modes of NHCs on oxide surfaces. In this work, we focus on the deposition of free NHCs, such as those generated by ex situ decarboxylation followed immediately by deposition [30]. The deposition of imidazolium salts [31, 32] or NHC-metal complexes [13–15] could lead to different trends, influenced by the presence of negatively charged counterions or mediated by the transition metal adatoms.

2 | Computational Details

Calculations were performed using the Vienna ab initio simulation code VASP 6 [40, 41]. Structural relaxations were conducted using the Perdew–Burke–Ernzerhof [42] exchange-correlation functional, with thresholds of 10^{-5} eV and 10^{-2} eV/Å for electronic and ionic loops, respectively. Long-range dispersion is included according to the D3 approach from Grimme, applying the Becke–Johnson damping function [43, 44]. Following structural relaxation, self-consistent single-point calculations were performed using the HSE06 + D3 hybrid functional to calculate the adsorption energies and electronic properties [45]. Core electrons were modeled with the projector augmented wave (PAW) method [46, 47], while H(1s), C(2s,2p), N(2s,2p), O(2s,2p), Mg(2p,3s), Si(2p,3s), Cu(3d,4s), and Ti(3p,4s) electrons were treated explicitly using a plane wave expansion up to a kinetic energy cut-off of 400 eV.

The MgO (001) surface was modeled with a three-layer slab. Cuprite Cu_2O (111) and rutile TiO_2 (110) surfaces were simulated with seven atomic-layer slabs. For SiO_2, we relied on a free-standing bilayer model widely used to study supported silica films [48]. For Cu_2O and TiO_2, the ionic coordinates of the three topmost layers were relaxed, while the ions from the four bottom layers were frozen in their bulk positions.

The optimized lattice parameters are as follows: for SiO_2, $a = b = 10.59$, $c = 4.39$, and $\gamma = 120.0°$; for MgO, $a = b = 8.92$, $c = 4.21$; for TiO_2, $a = 8.88$, $b = 6.53$, and $c = 9.26$. For Cu_2O 111, we considered a 2×2 supercell (12.05 Å × 12.05 Å). For unit cell optimizations of the surfaces and films, a k-point set of $(2 \times 2 \times 1)$ in the Monkhorst–Pack scheme was used for MgO. For all the Bis-IMe-Y–metal oxides models a, 2 ×2 supercells was adopted, in order to minimize the interctions between the adsorbd molecules. Reciprocal space sampling was reduced to the Γ point for the SiO_2 film, for Cu_2O and TiO_2 surfaces, and for all the Bis-IMe-Y–metal oxide models due to the large dimension of the supercells. A dipole correction was applied along the nonperiodic direction, and a vacuum clearance of at least 15 Å was included in the cells to avoid spurious interactions between periodic images.

The reported values of the Bader charges refer to the molecular adsorbates as the net charge transferred to or from the substrate upon adsorption. $Q < 0$ represents the electron density transferred to the surface from the adsorbate. $Q > 0$ represents the electron density transferred from the surface to the adsorbate.

3 | Results and Discussion

We extended the study to five different model NHCs (4-imidazolin-2-ylidene (H-Y, Figure 1A), 1,3-dimethyl-4-imidazolin-2-ylidene (IMe-Y, Figure 1B), bis(3-methyl-4-imidazolin-2-ylidene-1-yl)methane (Bis-IMe-Y, Figure 1C), the remote mesoionic 3,5-dimethylpyrazolium-4-ide (IMe-P, Figure 1D) and the nonremote mesoionic 1,3,4-trimethyl-1,2,3-triazolium-5-ide (IMe-T, Figure 1E) [23, 49]. Our selection of molecular substrates spans different structures of five-membered rings (bearing two or three N atoms and exhibiting neutral or mesoionic charge distribution) and different substituents (H or CH_3).

Depending on the molecular structure and steric hindrance, as well as the surface morphology of the metal oxides, six adsorption modes were identified, by analogy with previous works [50]: Upright surface configuration (Up_{surf}, Figure 1F), Upright Adatom configuration (Up_{ad}, Figure 1G), Tilted Surface configuration (T_{surf}, Figure 1H), Tilted Adatom configuration (T_{ad}, Figure 1I), Down Surface configuration ($Down_{surf}$, Figure 1J), and Down Adatom configuration ($Down_{ad}$, Figure 1K). Here, we report that in the same cases, NHC molecules induced reconstruction of the surface, and surface adatoms were spontaneously formed by extraction from the lattice surface, whereas extra-lattice species were not considered. For each molecule on each oxide surface, all possible adsorption modes were explored using GGA structure relaxations. Subsequently, single-point calculations with the hybrid functional HSE06 + D3 were performed

26894062, 2026, 10, Downloaded from https://onlinelibrary.wiley.com/doi/10.1002/sstr.70647 by CochraneItalia, Wiley Online Library on [23/10/2026]. See the Terms and Conditions (https://onlinelibrary.wiley.com/terms-and-conditions) on Wiley Online Library for rules of use; OA articles are governed by the applicable Creative Commons License

and are reported herein. The most relevant data are summarized in Tables 1, 2 and Figures 2–5; for further details, see also Table S1.

3.1 | NHCs Adsorption on Bare SiO_2 and MgO

The main results concerning the adsorption of the NHC molecules on SiO_2 and MgO are reported in Table 1 and Figure 2.

Starting from SiO_2, we report that only one stable adsorption mode was found, in which the carbene center interacts with a silicon atom (the Up_{surf} mode, Figure 2A–E). For H-Y (Figure 2A), the adsorption energy is weak (−0.65 eV, Table 1), and C—Si distance is 2.02 Å. The Si atom is pulled upward by 0.11 Å upon the formation of the C—Si bond. A very small positive charge is acquired by H-Y (+0.13 |e|). In the case of IMe-Y (with an Up_{surf} mode, Figure 2B), the binding energy is slightly smaller (−0.56 eV), the C-Si distance is slightly larger (2.09 Å), and the charge lost by the molecule is negligible

TABLE 1 | Support, NHC molecule, adsorption sites, calculated adsorption energies (D_e HSE06 + D3, eV), NHC-Metal bond lengths (Å), total Bader charges (Q, |e|) of the whole molecular adsorbates, and uplift of the lattice atom (Å) bound to NHC on silica and MgO.

Support	NHC	Binding site	D_e HSE06 + D3, eV	Bond length, Å	Q, |e|	Uplift, Å
SiO_2	H-Y	C—Si	−0.65	2.02	+0.13	+0.11
SiO_2	IMe-Y	C—Si	−0.56	2.09	+0.07	+0.13
SiO_2	Bis-IMe-Y	C—Si	−1.04	2.09	+0.01	+0.14
SiO_2	IMe-P	C—Si	−1.06	2.02	+0.14	+0.16
SiO_2	IMe-T	C—Si	−0.89	2.06	+0.13	+0.14
MgO	H-Y	C—Mg	−1.02	2.24	0.00	+0.15
MgO	IMe-Y	C—Mg	−1.03	2.38	−0.03	+0.26
MgO	Bis-IMe-Y	C—Mg/C—Mg	−3.89	2.43/2.42	−0.13	+0.22/+0.25
MgO	IMe-P	C—Mg	−1.24	2.28	−0.03	+0.26
MgO	IMe-T	C—Mg	−1.26	2.29	−0.06	+0.21

TABLE 2 | Support, NHC molecule, adsorption sites, calculated adsorption energies (D_e HSE06 + D3, eV), NHC–Metal bond lengths (Å), total Bader charges (Q, |e|) of the whole molecular adsorbates, and uplift of the lattice atom (Å) bound to NHC on bound to NHC on Cu_2O and TiO_2.

Support	NHC	Binding site	D_e HSE06 + D3, eV	Bond length, Å	Q, |e|	Uplift, Å
Cu_2O	H-Y	C—Cu1	−3.77	1.86	+0.26	+0.30
Cu_2O	H-Y	C—O	−3.17	1.28	+1.29	+2.43
Cu_2O	IMe-Y	C—Cu1	−3.27	1.88	+0.22	+0.73
Cu_2O	IMe-Y	C—O	−2.13	1.26	+1.27	+2.44
Cu_2O	Bis-IMe-Y	C—Cu1/C—Cu1	−4.96	1.90/1.86	+0.41	+0.61/+2.03
Cu_2O	Bis-IMe-Y	C—O/C—O	−4.79	1.87/1.23	+2.60	+1.01/+3.71
Cu_2O	IMe-P	C—Cu1	−3.78	1.88	−0.29	+0.60
Cu_2O	IMe-P	C—O	−1.88	1.33	+1.08	+0.11
Cu_2O	IMe-T	C—Cu1	−3.62	1.88	+ 0.28	+0.69
Cu_2O	IMe-T	C—O	−3.22	1.29	+1.28	+1.60
TiO_2	H-Y	C—Ti	−3.70	2.18	+0.24	−0.12
TiO_2	H-Y	C—O2	−4.08	1.27	+1.34	+0.00
TiO_2	IMe-Y	C—Ti	−3.20	2.27	+0.13	+0.28
TiO_2	IMe-Y	C—O2	−3.68	1.27	+1.31	+0.25
TiO_2	Bis-IMe-Y	C—Ti/C—Ti	−2.76	2.30/2.30	−0.02	+0.54/+0.53
TiO_2	Bis-IMe-Y	C—O2/C—O2	−6.15	1.27/1.27	+2.68	+0.49/+0.39
TiO_2	IMe-P	C—Ti	−3.77	2.21	+0.32	+0.30
TiO_2	IMe-P	C—O2	−3.64	1.30	+1.30	+0.08
TiO_2	IMe-T	C—Ti	−4.18	2.23	+0.21	+0.26
TiO_2	IMe-T	C—O2	−2.64	1.26	+1.30	+0.19

26884062, 2026, 10, Downloaded from https://onlinelibrary.wiley.com/doi/10.1002/sstr.70647 by CochraneItalia, Wiley Online Library on [23/10/2026]. See the Terms and Conditions (https://onlinelibrary.wiley.com/terms-and-conditions) on Wiley Online Library for rules of use; OA articles are governed by the applicable Creative Commons License

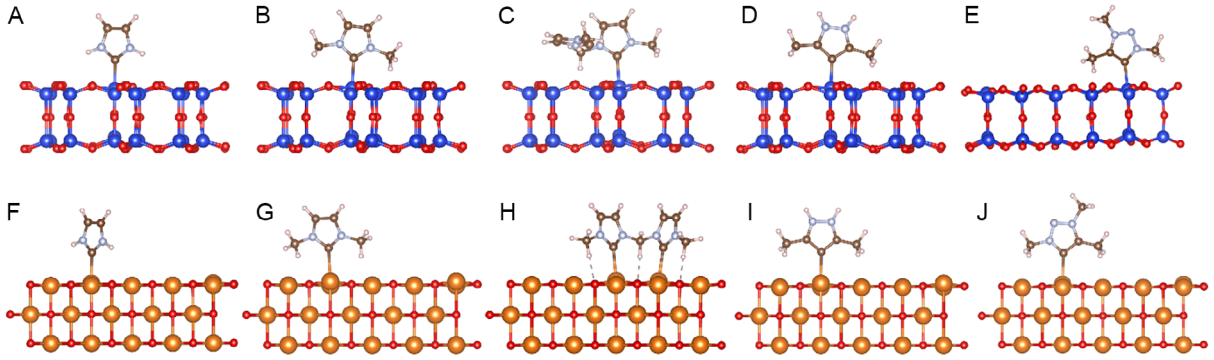


FIGURE 2 | Side views of the most stable adsorption sites detected on SiO_2, MgO, side view. Color code: C (brown), N (cyan), O (red), H (white), Si (blue), Mg (orange). Atomic configurations of the (A) H-Y, (B) IMe-Y, (C) Bis-IMe-Y, (D) IMe-P, and (E) IMe-T on silica oxide SiO_2 and atomic configurations of the (F) H-Y, (G) IMe-Y, (H) Bis-IMe-Y, (I) IMe-P, (J) IMe-T on magnesium oxide. Single-point with HSE06 + D3 at the PBE + D3 geometry's optimization.

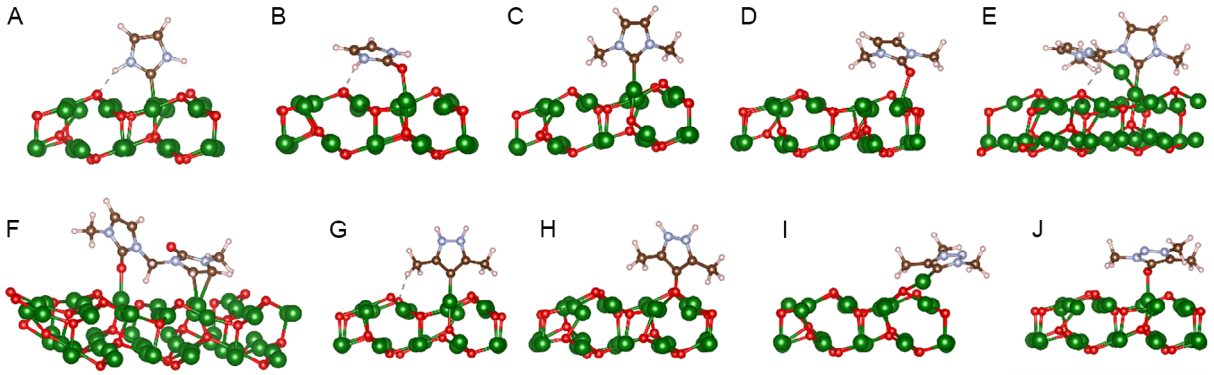


FIGURE 3 | Visual description of the most stable adsorption sites detected on Cu_2O, side view. Color code: C (brown), N (cyan), O (red), H (white), Cu (green). Only the top five atomic layers are reported for clarity. Single point with HSE06 + D3 at the PBE + D3 geometry's optimization.

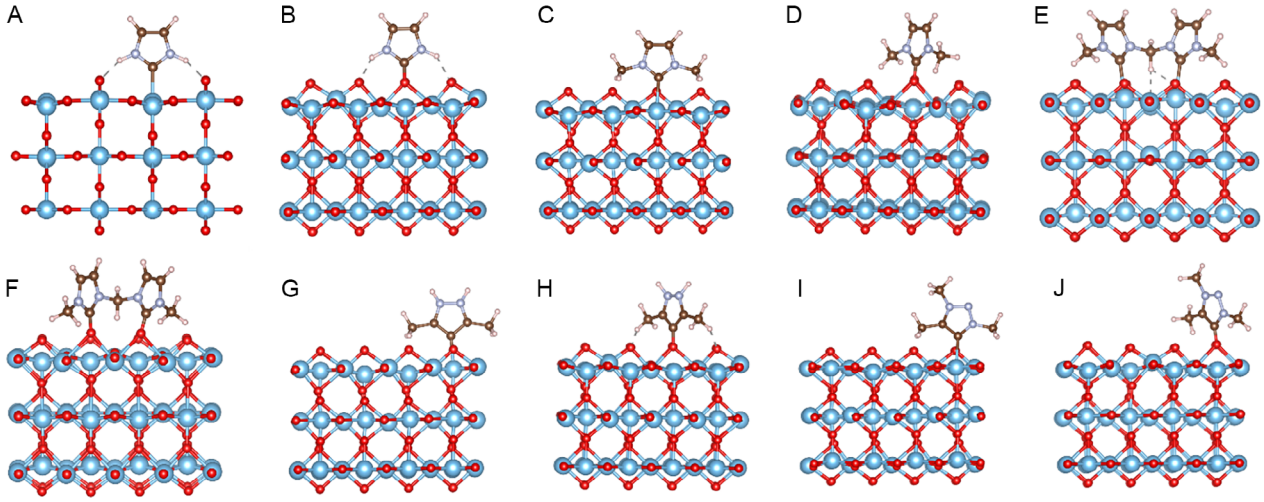


FIGURE 4 | Visual description of the most stable adsorption sites detected on TiO_2, side view. Color code: C (brown), N (cyan), O (red), H (white), Ti (blue sky). Single point with HSE06 + D3 at the PBE + D3 geometry's optimization.

(+0.07 |e|), Table 1. Overall, the NHC—silica bond looks very similar in the two cases. Both structural and energetic features reported here for IMe-Y closely resemble those observed for the same molecule on Si(111) [23, 49, 51], where IMe-Y is predicted to form a strong bond that preserves the carbene sp^2 character, resulting in an upright adsorption geometry. By directly comparing the DFT results, obtained with a very close computational setup in this paper and in previous studies [23, 49, 51], it can be seen that the adsorption energy on SiO_2 is almost four times weaker compared to Si(111) (−0.56 eV vs. almost −2 eV, as reported in ref. [51]). The strongly polar character of the Si—O bond thus negatively affects the Si bonding capability toward NHCs.

26884062, 2026, 10, Downloaded from https://onlinelibrary.wiley.com/doi/10.1002/sstr.70647 by CochraneItalia, Wiley Online Library on [23/10/2026]. See the Terms and Conditions (https://onlinelibrary.wiley.com/terms-and-conditions) on Wiley Online Library for rules of use; OA articles are governed by the applicable Creative Commons License

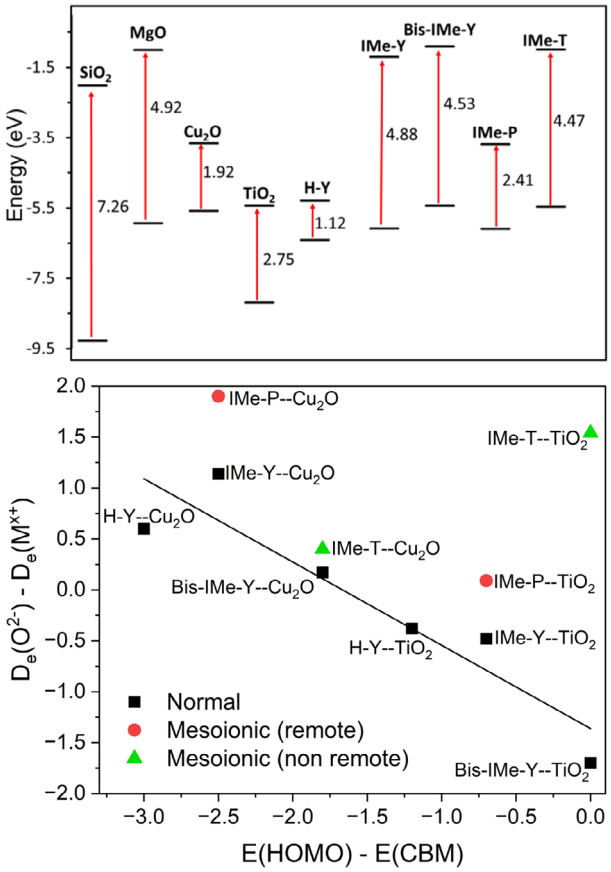


FIGURE 5 | Top: band alignment on slab models of oxide surfaces, band edges, and NHCs frontier orbitals. Bottom: difference in the adsorption energy on O^{2-} anions and M^{n+} metal cations (M = Cu, Ti) for NHCs on cuprite and titania, as a function of the energy difference between the HOMO of the NHC and the CBM of Cu_2O and TiO_2. Both orbital energies and adsorption energies are calculated with HSE06 + D3.

In a molecule featuring two carbene centers, such as Bis-IMe-Y Figure 1C, structural factors, such as the presence of two favorable surface sites at a distance compatible with the molecular structure, determine the final bonding geometry to the surface. On silica, this condition is not met, and Bis-IMe-Y is bound only through a single Si—C bond (Figure 2C). This behavior could also be a consequence of a poorer overlap with electron-accepting surface states caused by the electronic repulsions between the NHC molecule and the oxygen atoms (see Figure S1, comparing the structures of Bis-IMe-Y-SiO_2 and Bis-IMe-Y-MgO). The adsorption energy (−1.04 eV, Table 1) is larger than that of the mono-ring ylidene-like molecules owing to stabilizing dispersion interactions between the second ring and the silica surface, as observed by the structure where one of the two rings is in the Up_{surf} mode and the second one in the $Down_{surf}$ mode, with the phenyl ring parallel to the surface. The C—Si bond distance is equal to that in the IMe-Y case, and no charge transfer is observed (Table 1).

The remote mesoionic carbene, IMe-P (Figure 1D), displays a more pronounced nucleophilic character, which leads to a substantial increase in adsorption energy (−1.06 eV, Table 1 and an Up_{surf} mode) when carbene C binds to a surface Si atom (Figure 2D). The C—Si distance and charge transfer are in line with what was reported for the normal carbene. In the case of the nonremote mesoionic carbene IMe-T (Figures 1E and 2E), the adsorption energy (−0.89 eV, Table 1) lies between the values observed for the less nucleophilic normal carbenes (H-Y, IMe-Y, and Bis-IMe-Y) and the strongly nucleophilic remote mesoionic carbene IMe—P. Bond distance and charge transfer are analogous to the previous cases, as shown in Table 1, as well as the binding mode, i.e., Up_{surf} configuration mode is reported in Figure 2E. The small uplift of the Si atom bound to the carbene center is also consistent with the other NHCs.

The nucleophilic nature of the carbenes emerges even more prominently when the NHCs are bound to an exposed Mg^{2+} site on the MgO (001) surface. Similarly to silica, no stable binding modes other than C—Mg were identified for any of the considered NHCs on MgO. All the configurations obtained are reported in Table S1. Specifically, H-Y binds to an Mg surface site (Figure 2F, Up_{surf} mode) with an adsorption energy of −1.02 eV and a C—Mg distance of 2.24 Å (Table 1). Within the Bader formalism, no net charge is transferred to the molecule upon binding to the surface, suggesting an equivalence between donation and back-donation phenomena. IMe-Y, Figure 2G with an Up_{surf} mode, is bound with an almost identical adsorption energy (−1.03 eV, Table 1). The C—Mg distance is slightly larger compared to H-Y owing to the steric hindrance exerted by the side methyl substituents. In contrast to the behavior observed on silica, Bis-IMe-Y binds simultaneously to two Mg sites (in an Up_{surf} mode, Figure 2H), resulting in an adsorption energy (−3.89 eV, Table 1) that is more than double compared to IMe-Y. Indeed, the Mg–Mg distance at MgO (001) matches exactly the intramolecular spacing (2.42 and 2.43, Å, Table 1). The binding of IMe-Y to MgO has been recently experimentally reported by Ranganath et al. [52, 53], who performed a thorough spectroscopic and microscopic characterization under realistic working conditions for heterogeneous catalysis, confirming that NHCs are coordinated to Mg^{2+} sites.

The mesoionic carbenes also strongly bind to an Mg site with an Up_{surf} mode (−1.24 eV for IMe-P and −1.26 eV for IMe-T, Table 1 and Figure 2I,J) and with bonding distances and charge transfer values analogous to those reported for the normal carbenes. As expected, both mesoionic carbenes bind more strongly to MgO than to SiO_2. The uplift of the Mg^{2+} cation upon NHC binding is larger than that observed for silicon on silica.

The similar adsorption mechanism of NHCs on SiO_2 and MgO, involving the formation of a chemical bond between electrostatically positive surface sites (SiO_2 or MgO) and the carbene center with little to no charge transfer to the molecule, is further confirmed by the absence of spin density (Figures S2 and S3) and by the projected density of states, pDOS, Figures S4 and S5. For H-Y, for instance (Figures S2A and S4A for SiO_2 and S3A and S5A for MgO), the Highest Occupied Molecular Orbital (HOMO), exhibiting dominant C (2p) character, lies well below the Fermi level, which further supports the absence of charge transfer. More complex structures, such as Bis-IMe-Y, exhibit more complex features in the pDOS plot (Figures S4C and S5C), but the binding mode to the surface remains analogous.

3.2 | NHC Adsorption on Bare Cu_2O and TiO_2 Surfaces

On cuprite and titania, NHCs can bind to both metal sites (Cu and Ti) and oxygen anions, in contrast to what was reported for MgO and SiO_2 (Table 2 and Figures 3 and 4). Furthermore, we

26834062, 2026, 10, Downloaded from https://onlinelibrary.wiley.com/doi/10.1002/sstr.70647 by CochraneItalia, Wiley Online Library on [23/10/2026]. See the Terms and Conditions (https://onlinelibrary.wiley.com/terms-and-conditions) on Wiley Online Library for rules of use; OA articles are governed by the applicable Creative Commons License

highlight that in some cases, the binding of NHC molecules to the Cu_2O (111) surface involves the formation of oxygen or nonoxygen adatoms. These adatoms are supplied by forming a vacancy in the Cu_2O (111) surface.

On Cu_2O (111), all oxygen atoms are three-coordinated, while two distinct types of Cu sites exist: Cu1 (bound only to subsurface O species) and Cu2 (coordinated by both subsurface and surface O ions). The undercoordinated nature of Cu1 atoms renders them more reactive toward adsorbed molecules compared to Cu2. We thus focus in the main text (Table 2 and Figure 3) on the bonding of all NHCs with Cu1 and O sites. Cu2-NHC adducts are described in Table S1.

The most favorable adsorption mode for H-Y is on Cu1 in an Up_{surf} mode (Figure 3A), with a very large D_e of −3.77 eV and a short C—Cu bond distance of 1.86 Å, Table 2. The σ-donating nature of the chemical bond from carbene C to the Cu(3d) orbital is evidenced by the small, but non-negligible, positive charge acquired by the molecular substrate (+0.26 |e|, Table 2). H-Y binds to an O species in a $Down_{ad}$ mode on Cu_2O (111) with a smaller, but still substantial, D_e of −3.17 eV, as shown in Table 2 and Figure 3B. The C—O distance is 1.28, Å, compatible with a stretched carbonyl group in a cyclic urea molecule. The spontaneous extraction of an O atom from the surface induces the formation of a surface copper trimeric cluster with bond lengths of 2.43, 2.48, and 2.50 Å (Figure S6A), as was already reported by the effect of the interaction of the atomic H with the Cu_2O surface [54, 55]. In this case, the Bader charge is large and positive, +1.29 |e|. This indicates a more complex binding mode compared to the usual carbene–metal interaction: the molecular substrate is oxidized, while the surface is reduced as a result of extracting a formally neutral atomic O species, which binds to the NHC to form a cyclic urea and transfers two electrons to the oxide lattice. The absence of spin density in the oxide structure even after charge transfer, Figure S7, can be explained by the Mott–Hubbard nature of cuprite, where both VB and CB have predominant Cu(3d) character, as reported in earlier theoretical calculations [54, 55].

IMe-Y binds to cuprite in a manner comparable to H-Y; a stronger bond is obtained on Cu1 (D_e = −3.27 eV, Table 2 and Figure 3C) compared to O (D_e = −2.13 eV, Table 2 and Figure 3D). Charge transfer values analogous to H-Y are also reported (+0.22 |e| for IMe-Y–Cu_2O–Cu1 and +1.27 |e| for IMe-Y–Cu_2O–O, Table 2). The small decrease in D_e observed for IMe-Y/–Cu_2O–Cu1 with respect to H-Y–Cu_2O–Cu1 may stem from the steric hindrance of the methyl groups, whereas the much stronger decrease reported for IMe-Y–Cu_2O–O (−2.13 eV) with respect to H-Y–Cu_2O–O (−3.17 eV) may also be related to differences in the reconstruction induced in the cuprite by the oxygen vacancy creation.

For Bis-IMe-Y, all possible combinations of adsorption sites were considered (Cu1, Cu2, and O) for both carbene centers, see Supporting Information. The most stable adducts were formed when both carbene C atoms interact with Cu1 surface sites with an Up_{surf}/$Down_{ad}$ mode (Figure 3E), followed by the adsorption on two O sites and an Up_{surf}/$Down_{ad}$ mode (Figure 3F). Mixed CuO adsorption modes resulted in even less favorable, for more details, see Table S1. At variance with respect to what was observed for H-Y and IMe-Y, however, in the case of Bis-IMe-Y, the adsorption on two Cu1 sites (Figure 3E D_e = −4.96 eV) is only slightly favored over the adsorption on two O sites (Figure 3F D_e = −4.79 eV). The electronic charge transferred from Bis-IMe-Y is double the value reported for IMe-Y, while the C—Cu and C—O bond distances are nearly identical. This implies that the bis-carbene molecule can adjust its adsorption geometry on the cuprite surface to engage two highly favorable adsorption sites simultaneously.

The trends in stability (Cu1 > O) and charge transfer (minimal for Cu1 and substantial for O) observed for the normal NHCs are confirmed also for mesoionic NHCs. Specifically, a D_e of −3.78 eV is obtained for IMe-P on Cu1 (Figure 3G, Table 2, bound in an Up_{surf} mode), compared to a D_e of −1.88 eV for O (Figure 3H, Table 2, bound in an Up_{ad} mode). The bond distances (Table 2) are consistent with those observed for the normal NHCs; only the C—O bond distance is slightly larger, as expected from the tendency to localize a negative charge on the carbene center (Figure 1D). The sizeable increase in adsorption energy for IMe-P–Cu_2O–Cu1 compared to IMe-Y–Cu_2O–Cu1 confirms the stronger σ-donating characteristic of mesoionic NHCs [56]. IMe-T behaves similarly to IMe-P, with a slight decrease in D_e for bonding to both Cu1 (−3.62 eV, Table 2 and Figure 3I) and O (−3.22 eV, Figure 3J). The nonremote character of mesoionic IMe-T thus renders it slightly less reactive toward Cu_2O (111).

We now report the results of the NHCs adsorption on rutile TiO_2 (110). The surface morphology features equivalent five-coordinated Ti sites and two types of oxygen sites: two-coordinated oxygen (O2) and three-coordinated (O3) oxygen sites. The main text reports the results for the two most favorable sites for NHC adsorption, namely, O2 and Ti. Data concerning O3 can be found in Table S1.

As shown in Table 2 and Figure 4A,B, the largest adsorption energy for H-Y is obtained on O2 (−4.08 eV), followed by Ti (−3.70 eV). Notably, this trend is opposite to what was previously discussed for cuprite. The short C—O (1.27 Å) and C—Ti (2.18 Å) bond distances in Table 2 confirm the formation of strong bonds with the carbene molecule in both configurations. In both cases, H-Y is bound in an Up_{surf} mode (Figure 1F), i.e., no extraction of a surface species is observed but only a moderate uplift of the surface atom Table 2. On the contrary, the Ti—O distances in proximity to the bonding site results even slightly shorter compared to the clean surface. Consistent with the evidence previously discussed for MgO, silica, and cuprite, a small positive charge is acquired by the H-Y molecule upon adsorption on Ti, whereas a large positive charge (+1.34 |e|) is acquired upon binding to O. The reduction of the oxide substrate is clearly evident in the spin density plot (showing a net spin density spread on several Ti sites) and the pDOS, where occupied Ti(3d) states emerge in the gap (Figure S10a,b).

Switching from H-Y to IMe-Y (Figure 4C,D), the same stability trend is observed (D_e = −3.68 eV on O and −3.20 eV on Ti, Table 2) as well as the same binding mode. Once again, we attribute the smaller adsorption energies in the presence of bulkier side substituents to steric effects, as also shown by the slightly larger corresponding bond distances, as shown in Table 2. Features analogous to the H-Y case for spin density and pDOS are reported in Figure S10c,d.

Bis-IMe-Y can interact either with two O2 sites (D_e = −6.15 eV, Table 2 and Figure 4F) or with two Ti sites (D_e = −2.76 eV, Table 2 and Figure 4E). In both cases, the bonding abides by

26894062, 2026, 10, Downloaded from https://onlinelibrary.wiley.com/doi/10.1002/sstr.70647 by CochraneItalia, Wiley Online Library on [23/10/2026]. See the Terms and Conditions (https://onlinelibrary.wiley.com/terms-and-conditions) on Wiley Online Library for rules of use; OA articles are governed by the applicable Creative Commons License

an Up_{surf} mode. The adsorption energy reported for Bis-IMe-Y is remarkably smaller than twice the D_e of IMe-Y for both Ti and O sites. This indicates that the bidentate molecule undergoes significant structural distortion to bind two surface sites simultaneously. The Bader charges Table 2, confirm the trend described above: near-zero charge transfer upon adsorption on Ti and a very large positive charge acquired upon adsorption on O due to the formation of a cyclic urea molecule, as a result of the spontaneous extraction of an O atom from the surface. The actual reduction of titania in the latter case is confirmed by the spin density and the pDOS plot, as shown in Figure S10e,f.

The remote mesoionic carbene, IMe-P, behaves oppositely than the normal NHCs, exhibiting a slightly larger adsorption energy on Ti (−3.77 eV) than on O (−3.64 eV), Table 2 and Figure 4G,H. In both cases, an Up_{surf} mode is maintained. The strong σ-donating character of this molecule is reflected in the short C—Ti distance (2.21 Å) and the slightly larger Bader charge (+0.32 |e|) compared to the normal NHCs, as shown in Table 2. Clear fingerprints of the oxide reduction can again be identified in the spin density and pDOS plots,as shown in Figure S10g,h. The nonremote mesoionic IMe-T molecule, finally, displays a clear tendency toward binding on Ti ($D_e = -4.18$ eV) rather than O ($D_e = -2.64$ eV), Table 2 and Figure 4I,J with an Up_{surf} mode. No relevant differences in terms of bonding geometrical features and charge transfer are reported with respect to the preceding cases, as shown in Table 2.

3.3 | Electronic Factors Determining the Bonding Trends

The adsorption of NHCs on MgO, SiO_2, Cu_2O, and TiO_2, as discussed in the previous sections, reveals a nontrivial picture. A primary finding is that large gap nonreducible oxides (MgO and SiO_2) permit bonding exclusively to their positively charged surface sites, regardless of their more ionic (MgO) or covalent (silica) bonding nature. Vice versa, reducible oxides (cuprite and titania) accommodate both C-to-metal and C-to-O bonding modes.

Interestingly, while the bonding to Cu is always more favorable on cuprite, on titania, the mesoionic carbenes are preferentially bound to Ti, whereas the normal NHCs favor adsorption on O. Further differences among the NHCs emerge: mesoionic NHCs are more strongly bound to Mg- and Si-sites compared to normal NHCs. The steric effects of the side groups (often also referred to as wingtips) are evidenced by the generally smaller adsorption energies of methyl-substituted ylidene (IMe-Y) compared to those of H-Y. As shown by previous works on the deposition of NHCs with very large di-iso-propyl-phenyl side groups on oxidized Cu, however, the steric hindrance can become the dominant factor directing the binding toward smaller O atoms compared to larger Cu [29–31].

The most complex factor to rationalize is, however, the electronic structure. To this end, we report in Figure 5 (top panel) the band edges of the investigated oxides alongside the energy of the NHCs frontier orbitals, all calculated with HSE06 + D3 and consistently aligned with respect to the vacuum level, for direct comparison. The oxide band edges were calculated on slab models and are thus relative to the specific facets and surface terminations. The silica surface possesses a very large gap (7.26 eV at the HSE06 level), followed by MgO (close to 5 eV with HSE06). These oxides are very hard to reduce because a sizeable electron transfer into their conduction bands would require populating states at very high energy. This energetic barrier excludes the NHCs binding to O. The larger adsorption energies observed on MgO compared to those on SiO_2 can be attributed to the more pronounced positive character of the Mg surface sites.

Cuprite and titania display a reducible nature as evidenced by their substantially smaller bandgaps. However, in Figure 5 top panel, titania's band edges (valence band maximum, VBM, and conduction band minimum, CBM) are located at remarkably lower energy compared to those from cuprite. As previously discussed, the presence of empty states at low energy is determinant for oxide reducibility [57]. On cuprite, thus, bonding to O is possible, but the high-lying CBM disfavors it compared to bonding to Cu for all NHCs. Only Bis-IMe-Y was used, i.e., the NHC with the highest-lying HOMO, which displays nearly equal binding to O and to Cu. Moreover, Bis-IMe-Y, as a bis-carbene, introduces relevant structural constraints which can influence its adsorption, such as the match between the carbene–carbene distance and the peculiar surface morphology of each oxide.

A distinct trend emerges for titania and cuprite, where bonding to O is also possible; on Cu_2O, bonding to Cu is favored over bonding to O, while on TiO_2, bonding to O is more favorable for normal NHCs, whereas mesoionic NHCs prefer bonding to Ti.

A second factor to consider is the electronic structure of the molecule: the higher the HOMO energy, the more prone the NHC is to donate charge-forming bonds to O.

Indeed, in the case of normal NHCs, as shown in Figure 5 (bottom), a stronger preference for binding to O emerges when the NHC HOMO is shallower. The CB of cuprite is much higher in energy compared to that of titania, and this destabilizes bonding to oxygen. One must consider, moreover, that once the bond is formed, the electronic structure of titania will relax, and the state hosting them will be in a deeper position in the oxide gap, as shown in the DOS Figure S10. Interestingly, remote and nonremote mesoionic carbenes follow different trends: the remote mesoionic carbene, i.e., IMe-P, displays a more favorable bonding to O on titania compared to cuprite, like normal NHCs. Nonremote IMe-T displays the opposite trend. It is evident that the charge dislocation within the ring is also very relevant to the bonding mode of NHCs, and an extensive study in the future will be necessary to derive a comprehensive trend for mesoionic NHCs.

It is interesting to note that the mesoionic NHCs have HOMOs at energies comparable to those of normal NHCs. Their stronger σ-donating nature, thus, can be attributed to the different capabilities of charge redistribution on the ring structure *via* resonance as shown in Figure 1.

This complex picture, thus, is both oxide-dependent and NHC-dependent. It is interesting to note that in a previous experimental work [31], where an imidazol-derived NHC, sporting bulky aromatic wingtips and electron-withdrawing substituents, was adsorbed on CuO_x, TiO_x, and FeO_x thin films, a different trend emerged (namely, bonding to Ti on TiO_x, to O on CuO_x, and mixed bond on FeO_x). As previously discussed, this discrepancy may stem from the inherent difference between depositing imidazolium salts, as in Ref. [31] *versus* neutral carbenes, as discussed here.

26894062, 2026, 10, Downloaded from https://onlinelibrary.wiley.com/doi/10.1002/sstr.70647 by CochraneItalia, Wiley Online Library on [23/10/2026]. See the Terms and Conditions (https://onlinelibrary.wiley.com/terms-and-conditions) on Wiley Online Library for rules of use; OA articles are governed by the applicable Creative Commons License

Finally, a very important methodological caveat must be reported. The orbital and band alignments reported in Figure 5 are very sensitive to the choice of the exchange-correlation functional. GGA functionals, for instance, are very reliable in describing the structural features of molecules on surfaces but tend to underestimate the bandgap of most oxides [58], which could spuriously favor binding modes involving the reduction of the oxidic support. To prevent this, we refined the structural relaxation performed by GGA, carrying out single-point calculations with the HSE06 + D3 hybrid functional. This approach ensures that our calculations of adsorption energies and relative stabilities rely on correct band edges and frontier orbital alignment. Nevertheless, as seen in the Supporting Information, a peculiar feature emerges in the case of titania: when NHCs bind to O and electrons are transferred to TiO_2, the related spin density is delocalized on several Ti atoms. Most likely, charge localization would be observed if one relaxed the whole structure with HSE06. As thoroughly discussed in the past, however, the localized *versus* delocalized description of the reduced centers in titania has a negligible effect on the total electronic energy [59], allowing us to rely on the relative stabilities evaluated with our approach.

4 | Conclusions

In this work, we studied the adsorption of five different NHCs on various oxide surfaces: two normal single-ring NHCs, differing in their side groups (H and CH_3), a bis-carbene, and two mesoionic carbenes (one remote and one nonremote). We sampled four different oxide surfaces, comprising nonreducible (silica and MgO) and reducible (cuprite and titania) oxides. All considered oxides hold significant practical implications as functionalization supports, with promising applications in various fields (catalysis, electrochemistry, sensing, theranostics, and microelectronics).

Recurring to hybrid single-point DFT calculations on structures relaxed with GGA, we demonstrated that NHCs can bind either to positive surface sites (Si or metal cations) or to oxygen. Bonding to Si and metal cations involves competing charge donation and back-donation mechanisms, which eventually leave the adsorbed NHCs slightly positively charged or near-neutral. The bonding to O and the concomitant formation of a cyclic urea implies the reduction of the oxidic support.

Oxide reducibility is thus the primary factor dictating the bonding mode of NHCs, with C-to-O bonding occurring exclusively on reducible oxides. The preference for this bonding is more pronounced in the presence of a low-lying CB edge.

The molecular electronic structure plays a twofold role: on the one hand, NHCs with shallow HOMOs are more prone to electron donation via C-to-O bonding. On the other hand, the capacity to delocalize the charge across the heterocycle is a decisive factor in favoring bonding to surface oxygen. Mesoionic carbenes, in which charge delocalization is restricted, exhibit a more pronounced nucleophilic character when brought into contact with oxide surfaces.

NHCs are thus versatile molecules whose bonding mode can be tuned by controlling their electronic and steric features. This work paves the way toward the rational design of tailored molecule/surface assemblies, where properties such as the concentration of charge carriers in the oxide and the interfacial dipole moment can be effectively modulated.

Acknowledgments

We acknowledge financial support from the Fondazione Cariplo, grant 2022-0713 PLANET. This work has also been funded within the framework of the Regional Programme of the European Regional Development Fund 2021–2027 of Regione Lombardia (PR FESR 2021–2027, Action 1.1.3, in compliance with European Regulation No. 1060/2021), following the public call "Collabora&Innova". Project "CO_2: from a global problem to a tool to implement circularity—CO-Tool" (Project ID 6144755). The support of CINECA for computational resources is also kindly acknowledged. We are grateful to Andrea Biffis, (University of Padova), Sara Mattiello (University of Milano-Bicocca), Juan Navarro and Markus Heyde (Fritz-Haber Institute of the Max Planck Society), and Frank Glorius (University of Münster) for insightful discussions.

Funding

This study was supported by the Fondazione Cariplo (2022-0713 PLANET) and Regione Lombardia (PR FESR 2021-2027, Action 1.1.3, in compliance with European, Regulation No. 1060/2021).

Conflicts of Interest

The authors declare no conflicts of interest.

Data Availability Statement

The data that support the findings of this study are available from the corresponding author upon reasonable request.

References

1. M. J. MacLeod, A. J. Goodman, H. Z. Ye, H. V. T. Nguyen, T. Van Voorhis, and J. A. Johnson, "Robust Gold Nanorods Stabilized by Bidentate N-Heterocyclic-Carbene–Thiolate Ligands," *Nature Chemistry* 11, no. 1 (2019): 57–63, https://doi.org/10.1038/s41557-018-0159-8.

2. C. A. Smith, M. R. Narouz, P. A. Lummis, et al., "*N* -Heterocyclic Carbenes in Materials Chemistry," *Chemical Reviews* 119, no. 8 (2019): 4986–5056, https://doi.org/10.1021/acs.chemrev.8b00514.

3. G. Kaur, R. L. Thimes, J. P. Camden, and D. M. Jenkins, "Fundamentals and Applications of N-Heterocyclic Carbene Functionalized Gold Surfaces and Nanoparticles," *Chemical Communications* 58, no. 95 (2022): 13188–13197, https://doi.org/10.1039/d2cc05183d.

4. A. V. Zhukhovitskiy, M. J. MacLeod, and J. A. Johnson, "Carbene Ligands in Surface Chemistry: From Stabilization of Discrete Elemental Allotropes to Modification of Nanoscale and Bulk Substrates," *Chemical Reviews* 115, no. 20 (2015): 11503–11532, https://doi.org/10.1021/acs.chemrev.5b00220.

5. P. Bellotti, M. Koy, M. N. Hopkinson, and F. Glorius, "Recent Advances in the Chemistry and Applications of N-Heterocyclic Carbenes," *Nature Reviews Chemistry* 5, no. 10 (2021): 711–725, https://doi.org/10.1038/s41570-021-00321-1.

6. M. Voccia, S. P. Nolan, L. Cavallo, and A. Poater, "The Activity of Indenylidene Derivatives in Olefin Metathesis Catalysts," *Beilstein Journal of Organic Chemistry* 14 (2018): 2956–2963, https://doi.org/10.3762/bjoc.14.275.

7. V. M. Chernyshev, E. A. Denisova, D. B. Eremin, and V. P. Ananikov, "The Key Role of R—NHC Coupling (R═C, H, Heteroatom) and M-NHC Bond Cleavage in the Evolution of M/NHC Complexes and Formation of Catalytically Active Species," *Chemical Science* 11, no. 27 (2020): 6957–6977, https://doi.org/10.1039/d0sc02629h.

8. A. Brotons-Rufes, S. Posada-Pérez, J. P. Martínez, S. P. Nolan, and A. Poater, "Challenges in Olefin Metathesis: Past, Present and Future," *Coordination Chemistry Reviews* 542 (2025): 216827, https://doi.org/10.1016/j.ccr.2025.216827.

26884062, 2026, 10, Downloaded from https://onlinelibrary.wiley.com/doi/10.1002/sstr.70647 by CochraneItalia, Wiley Online Library on [23/10/2026]. See the Terms and Conditions (https://onlinelibrary.wiley.com/terms-and-conditions) on Wiley Online Library for rules of use; OA articles are governed by the applicable Creative Commons License

9. M. Voccia, L. Falivene, L. Cavallo, C. Tubaro, A. Biffis, and L. Caporaso, "Ligand Effects in Pd-Catalyzed Intermolecular Alkyne Hydroarylations," *Organometallics* 38, no. 19 (2019): 3730–3739, https://doi.org/10.1021/acs.organomet.9b00473.

10. M. N. Hopkinson, C. Richter, M. Schedler, and F. Glorius, "An Overview of N-Heterocyclic Carbenes," *Nature* 510, no. 7506 (2014): 485–496, https://doi.org/10.1038/nature13384.

11. S. Ikemoto, S. Muratsugu, T. Koitaya, et al., "Coordination-Induced Trigger for Activity: N-Heterocyclic Carbene-Decorated Ceria Catalysts Incorporating Cr and Rh With Activity Induction by Surface Adsorption Site Control," *Journal of the American Chemical Society* 145, no. 3 (2023): 1497–1504, https://doi.org/10.1021/jacs.2c07290.

12. J. V. Musso, J. De Jesus Silva, M. J. Benedikter, et al., "Cationic Molybdenum Oxo Alkylidenes Stabilized by N-Heterocyclic Carbenes: From Molecular Systems to Efficient Supported Metathesis Catalysts," *Chemical Science* 13, no. 29 (2022): 8649–8656, https://doi.org/10.1039/d2sc03321f.

13. M. Ghosh and S. Khan, "N-Heterocyclic Carbenes Capped Metal Nanoparticles: An Overview of Their Catalytic Scope," *ACS Catalysis* 13, no. 14 (2023): 9313–9325, https://doi.org/10.1021/acscatal.3c01824.

14. J. F. Soulé, H. Miyamura, and S. Kobayashi, "Copolymer-Incarcerated Nickel Nanoparticles With *N*-Heterocyclic Carbene Precursors as Active Cross-Linking Agents for Corriu-Kumada-Tamao Reaction," *Journal of the American Chemical Society* 135, no. 29 (2013): 10602–10605, https://doi.org/10.1021/ja404006w.

15. H. Min, H. Miyamura, S. Kobayashi, "N-Heterocyclic Carbene Coordinated Heterogeneous Pd Nanoparticles as Catalysts for Suzuki-Miyaura Coupling," *Chemistry Letters* 45, no. 7 (2016): 837–839, https://doi.org/10.1246/cl.160369.

16. P. Tegeder, M. Marelli, M. Freitag, et al., "Metal Vapor Synthesis of Ultrasmall Pd Nanoparticles Functionalized With N-Heterocyclic Carbenes," *Dalton Transactions* 47, no. 36 (2018): 12647–12651, https://doi.org/10.1039/c8dt02535e.

17. L. Rakers, L. M. Martínez-Prieto, A. M. López-Vinasco, et al., "Ruthenium Nanoparticles Ligated by Cholesterol-Derived NHCs and Their Application in the Hydrogenation of Arenes," *Chemical Communications* 54, no. 51 (2018): 7070–7073, https://doi.org/10.1039/c8cc02833h.

18. A. Lv, M. Freitag, K. M. Chepiga, A. H. Schäfer, F. Glorius, and L. Chi, "Mit N-heterocyclischen Carbenen behandelte Goldoberflächen in Pentacen-Transistoren: Verbesserte Stabilität und Kontakt an der Grenzfläche," *Angewandte Chemie* 130, no. 17 (2018): 4883–4887, https://doi.org/10.1002/ange.201713415.

19. D. T. Nguyen, M. Freitag, C. Gutheil, et al., "An Arylazopyrazole-Based N-Heterocyclic Carbene as a Photoswitch on Gold Surfaces: Light-Switchable Wettability, Work Function, and Conductance," *Angewandte Chemie, International Edition* 59, no. 32 (2020): 13651–13656, https://doi.org/10.1002/anie.202003523.

20. Z. Wang, M. Das, C. Gutheil, et al., "Surface Modification With a Fluorinated N-Heterocyclic Carbene on Au: Effect on Contact Resistance in Organic Field-Effect Transistors," *Journal of Materials Chemistry C* 10, no. 22 (2022): 8589–8595, https://doi.org/10.1039/d2tc01311h.

21. G. P. Moss, P. A. S. Smith, and D. Tavernier, "Glossary of Class Names of Organic Compounds and Reactivity Intermediates Based on Structure (IUPAC Recommendations 1995)," *Pure and Applied Chemistry* 67, no. 8-9 (1995): 1307–1375, https://doi.org/10.1351/pac199567081307.

22. R. H. Crabtree, "Abnormal, Mesoionic and Remote N-Heterocyclic Carbene Complexes," *Coordination Chemistry Reviews* 257, no. 3-4 (2013): 755–766, https://doi.org/10.1016/j.ccr.2012.09.006.

23. O. Schuster, L. Yang, H. G. Raubenheimer, and M. Albrecht, "Beyond Conventional *N*-Heterocyclic Carbenes: Abnormal, Remote, and Other Classes of NHC Ligands With Reduced Heteroatom Stabilization," *Chemical Reviews* 109, no. 8 (2009): 3445–3478, https://doi.org/10.1021/cr8005087.

24. D. S. Lee, I. Singh, A. J. Veinot, et al., "Mesoionic Carbene-Based Self-Assembled Monolayers on Gold," *Chemical Science* 15, no. 7 (2024): 2480–2485, https://doi.org/10.1039/d3sc04720b.

25. E. Peris and R. H. Crabtree, "Recent Homogeneous Catalytic Applications of Chelate and Pincer N-Heterocyclic Carbenes," *Coordination Chemistry Reviews* 248, no. 21–24 (2004): 2239–2246, https://doi.org/10.1016/j.ccr.2004.04.014.

26. E. Peris and R. H. Crabtree, "New Routes to Carbene Complexes for Thermally and Oxidatively Robust Homogeneous Catalysts," *Comptes Rendus. Chimie* 6, no. 1 (2003): 33–37, https://doi.org/10.1016/S1631-0748(03)00003-1.

27. E. Peris, J. A. Loch, J. Mata, and R. H. Crabtree, "A Pd Complex of a Tridentate Pincer CNC Bis-Carbene Ligand as a Robust Homogenous Heck Catalyst," *Chemical Communications* 37, no. 2 (2001): 201–202, https://doi.org/10.1039/b008038l.

28. A. J. Veinot, A. Al-Rashed, J. D. Padmos, et al., "N-Heterocyclic Carbenes Reduce and Functionalize Copper Oxide Surfaces in One Pot," *Chemistry – A European Journal* 26, no. 50 (2020): 11431–11434, https://doi.org/10.1002/chem.202002308.

29. J. Navarro, M. Das, S. Tosoni, et al., "Promoted Thermal Reduction of Copper Oxide Surfaces by N-Heterocyclic Carbenes," *Journal of Physical Chemistry C* 126, no. 41, 17528–17535, https://doi.org/10.1021/acs.jpcc.2c04257.

30. J. Navarro, M. Das, S. Tosoni, et al., "Covalent Adsorption of N-Heterocyclic Carbenes on a Copper Oxide Surface," *Journal of the American Chemical Society* 144, no. 36, 16267–16271, https://doi.org/10.1021/jacs.2c06335.

31. E. Amit, R. Mondal, I. Berg, Z. Nairoukh, and E. Gross, "N-Heterocyclic Carbene Monolayers on Metal-Oxide Films: Correlations Between Adsorption Mode and Surface Functionality," *Langmuir* 40, no. 19 (2024): 10374–10383, https://doi.org/10.1021/acs.langmuir.4c01109.

32. K. Salorinne, R. W. Y. Man, C.H. Li, M. Taki, M. Nambo, and C. M. Crudden, "Water-Soluble N-Heterocyclic Carbene-Protected Gold Nanoparticles: Size-Controlled Synthesis, Stability, and Optical Properties," *Angewandte Chemie* 129, no. 22 (2017): 6294–6298, https://doi.org/10.1002/ange.201701605.

33. M. Das, M. Kohlstädt, M. Enders, et al., "Surface Modification of ITO With N-Heterocyclic Carbene Precursors Results in Electron Selective Contacts in Organic Photovoltaic Devices," *Chemistry – A European Journal* 29, no. 60 (2023): e202301482, https://doi.org/10.1002/chem.202301482.

34. N. Kaeffer, D. Mance, and C. Copéret, "N-Heterocyclic Carbene Coordination to Surface Copper Sites in Selective Semihydrogenation Catalysts From Solid-State NMR Spectroscopy," *Angewandte Chemie, International Edition* 59, no. 45 (2020): 19999–20007, https://doi.org/10.1002/anie.202006209.

35. S. Dery, W. Cao, C. Yao, and C. Copéret, "NMR Spectroscopic Signatures of Cationic Surface Sites From Supported Coinage Metals Interacting With N-Heterocyclic Carbenes," *Journal of the American Chemical Society* 146, no. 10 (2024): 6466–6470, https://doi.org/10.1021/jacs.4c00200.

36. M. I. Qadir, C. P. Ebersol, B. A. da Silva, et al., "Hidden Carbenes: NHC-Al Species at the Al_2O_3–Ionic Liquid Interface," *JACS Au* 5, no. 9 (2025): 4370–4377, https://doi.org/10.1021/jacsau.5c00736.

37. J. Sauer and H. J. Freund, "Models in Catalysis," *Catalysis Letters* 145, no. 1 (2015): 109–125, https://doi.org/10.1007/s10562-014-1387-1.

38. D. Gao, R. M. Arán-Ais, H. S. Jeon, and B. Roldan Cuenya, "Rational Catalyst and Electrolyte Design for CO_2 Electroreduction Towards Multicarbon Products," *Nature Catalysis* 2, no. 3 (2019): 198–210, https://doi.org/10.1038/s41929-019-0235-5.

26884062, 2026, 10, Downloaded from https://onlinelibrary.wiley.com/doi/10.1002/sstr.70647 by CochraneItalia, Wiley Online Library on [23/10/2026]. See the Terms and Conditions (https://onlinelibrary.wiley.com/terms-and-conditions) on Wiley Online Library for rules of use; OA articles are governed by the applicable Creative Commons License

39. J. Navarro, S. Tosoni, J. Bruce, et al., "Structure of a Silica Thin Film on Oxidized Cu(111): Conservation of the Honeycomb Lattice and Role of the Interlayer," *Journal of Physical Chemistry C* 124, no. 38 (2020): 20942–20949, https://doi.org/10.1021/acs.jpcc.0c05463.

40. G. Kresse and B' J. Furthmiiller, "Efficiency of Ab-Initio Total Energy Calculations for Metals and Semiconductors Using a Plane-Wave Basis Set," *Computational Materials Science* 6, no. 1 (1996): 15-50, https://doi.org/10.1016/0927-0256(96)00008-0.

41. G. Kresse and J. Furthmü, "Efficient Iterative Schemes for Ab Initio Total-Energy Calculations Using a Plane-Wave Basis Set," *Physical review B* 54, no. 16-15 (1996): 11169-11186.

42. J. P. Perdew, K. Burke, and M. Ernzerhof, "Generalized Gradient Approximation Made Simple," *Physical review letters* 77, no. 18 (1997): 3865-3868, https://doi.org/10.1103/PhysRevLett.77.3865.

43. S. Grimme, S. Ehrlich, and L. Goerigk, "Effect of the Damping Function in Dispersion Corrected Density Functional Theory," *Journal of Computational Chemistry* 32, no. 7 (2011): 1456–1465, https://doi.org/10.1002/jcc.21759.

44. S. Grimme, J. Antony, S. Ehrlich, and H. Krieg, "A Consistent and Accurate *ab initio* Parametrization of Density Functional Dispersion Correction (DFT-D) for the 94 elements H-Pu," *Journal of Chemical Physics* 132, no. 15 (2010), https://doi.org/10.1063/1.3382344.

45. J. Heyd, G. E. Scuseria, and M. Ernzerhof, "Erratum: Hybrid Functionals Based on a Screened Coulomb Potential (Journal of Chemical Physics (2003) 118 (8207))" *Journal of Chemical Physics* 124, no. 21 (2006): 219906, https://doi.org/10.1063/1.2204597.

46. P. E. Blochl, "Projector Augmented-+rave Method," *Physical review B* 50, no. 24 (1994): 17953-17979, https://doi.org/10.1103/PhysRevB.50.17953.

47. G. Kresse and D. Joubert, "From Ultrasoft Pseudopotentials to the Projector Augmented-Wave Method," *Physical review B* 59, no. 3 (1999): 1758-1775, https://doi.org/10.1103/PhysRevB.

48. A. L. Lewandowski, P. Schlexer, S. Tosoni, et al., "Determination of Silica and Germania Film Network Structures on Ru(0001) at the Atomic Scale," *Journal of Physical Chemistry C* 123, no. 13 (2019): 7889–7897, https://doi.org/10.1021/acs.jpcc.8b07110.

49. Á. Vivancos, C. Segarra, and M. Albrecht, "Mesoionic and Related Less Heteroatom-Stabilized N-Heterocyclic Carbene Complexes: Synthesis, Catalysis, and Other Applications," *Chemical Reviews* 118, no. 19 (2018): 9493–9586, https://doi.org/10.1021/acs.chemrev.8b00148.

50. C. Gutheil, G. Roß, S. Amirjalayer, et al., "Tailored Monolayers of N-Heterocyclic Carbenes by Kinetic Control," *ACS Nano* 18, no. 4 (2024): 3043–3052, https://doi.org/10.1021/acsnano.3c08045.

51. M. Franz, S. Chandola, M. Koy, et al., "Controlled Growth of Ordered Monolayers of N-Heterocyclic Carbenes on Silicon," *Nature Chemistry* 13, no. 9 (2021): 828–835, https://doi.org/10.1038/s41557-021-00721-2.

52. M. Shaikh, M. Sahu, S. Khilari, A. K. Kumar, P. Maji, and K. V. S. Ranganath, "Surface Modification of Polyhedral Nanocrystalline MgO With Imidazolium Carboxylates for Dehydration Reactions: A New Approach," *RSC Advances* 6, no. 86 (2016): 82591–82595, https://doi.org/10.1039/c6ra16358k.

53. M. Shaikh, M. Sahu, P. K. Gavel, et al., "Mg-NHC Complex on the Surface of Nanomagnesium Oxide for Catalytic Application," *Catalysis Communications* 84 (2016): 89–92, https://doi.org/10.1016/j.catcom.2016.06.007.

54. Y. W. Ching, Y. N. Xu, and K. W. Wong, "Ground-State and Optical Properties of Cu & O and CuO Crystals," *Physical review B* 40, no. 11 (1989): 7684- 7695, https://doi.org/10.1103/PhysRevB.40.7684.

55. P. Marksteiner, P. Blaha, and K. Schwarz, "Condensed Matter for Physik B Electronic Structure and Binding Mechanism of CuzO," *Zeitschrift für Physik B Condensed Matter* 64 (1986): 119-127, https://doi.org/10.1007/BF01303692.

56. D. Martin, M. Melaimi, M. Soleilhavoup, and G. Bertrand, "A Brief Survey of Our Contribution to Stable Carbene Chemistry," *Organometallics* 30, no. 20 (2011): 5304–5313, https://doi.org/10.1021/om200650x.

57. Z. Helali, A. Jedidi, O. A. Syzgantseva, M. Calatayud, and C. Minot, "Scaling Reducibility of Metal Oxides," *Theoretical Chemistry Accounts* 136, no. 9 (2017): 100, https://doi.org/10.1007/s00214-017-2130-y.

58. J. P. Perdew, W. Yang, K. Burke, et al., "Understanding Band Gaps of Solids in Generalized Kohn–Sham Theory," *Proceedings of the National Academy of Sciences* 114, no. 11 (2017): 2801–2806, https://doi.org/10.1073/pnas.1621352114.

59. C. Di Valentin, G. Pacchioni, and A. Selloni, "Reduced and n-Type Doped TiO_2: Nature of Ti^{3+} Species," *Journal of Physical Chemistry C* 113, no. 48 (2009): 20543–20552, https://doi.org/10.1021/jp9061797.

Supporting Information

Additional supporting information can be found online in the Supporting Information section.

26894062, 2026, 10, Downloaded from https://onlinelibrary.wiley.com/doi/10.1002/sstr.70647 by CochraneItalia, Wiley Online Library on [23/10/2026]. See the Terms and Conditions (https://onlinelibrary.wiley.com/terms-and-conditions) on Wiley Online Library for rules of use; OA articles are governed by the applicable Creative Commons License